Measurement 256 (2025) 118444



Contents lists available at ScienceDirect

Measurement

journal homepage: www.elsevier.com/locate/measurement



Temperature-tunable Fabry-Pérot filter for miniaturization of high-resolution spectrometers

Bruno Esteves [a,*], Bernardo Santos Dores [a,b], Manuel Fernando Silva [a,b], José Higino Correia [a,b], José Artur Rodrigues [a,b]

[a] CMEMS-UMinho, University of Minho, 4800-058 Guimarães, Portugal
[b] Labbels – Associate Laboratory, Braga/Guimarães, Portugal

ARTICLE INFO

Keywords:
Fabry-Pérot
Tunable optical filter
Brillouin spectroscopy
Glass resonance cavity
Temperature modulation

ABSTRACT

This study introduces a new method for implementing large-gap, tunable Fabry-Pérot interferometers for high-resolution spectroscopy. The process utilizes solid resonance cavities obtained from commonly available, unaltered glass substrates. The transmitted wavelength is controlled via the thermo-optic effect and thermal expansion instead of intricate mechanical systems, streamlining miniaturization and enhancing device integration. Experimental results show a transmission wavelength shift of 5.7 pm/°C for a free spectral range of 137.1 pm, using 700 μm solid glass cavities. Exceptional linearity was observed, ensuring precise and predictable wavelength control. This concept was motivated by the need for miniaturizing Brillouin spectroscopy signal acquisition, which requires filters with extraordinary spectral resolution. The commonly used tunable Fabry-Pérot filter systems rely on complex piezoelectric-based actuators to adjust mirror spacing and alignment, making them impractical. The proposed alternative may lead to highly accurate, high-resolution, and low-maintenance filters, ideal for miniaturized spectrometry applications.

1. Introduction

Brillouin scattering is a type of inelastic scattering that occurs when photons interact with the acoustic phonons and magnons in a material, inducing a wavelength shift [1,2]. The resulting shifts are in the 0.1–100 GHz range and provide information about the viscoelastic properties of the target material [3]. This proximity to the Rayleigh peak, combined with an intensity several orders of magnitude lower, exemplifies how difficult it can be to detect and quantify this type of signal.

Current state-of-the-art Brillouin spectrometers have enough resolution to probe the viscoelastic properties of materials and tissues with sufficient quality to find applications in several industries, such as material sciences, food, and medical field [4–7]. However, despite their versatility and utility, traditional spectroscopy setups often rely on bulky and complex filtering systems to achieve the spectral resolution necessary for accurate measurements. Among these systems, tandem air–gap Fabry-Pérot filters achieve the highest resolution and contrast by leveraging precise piezoelectric actuators to adjust mirror spacing and alignment. This causes high sensitivity to vibrations that coupled with the challenges of using complex actuators, making miniaturization and integration challenging [8].

In contexts such as medical diagnostics, where instrumentation size plays a critical role in device integration and usability, the limitations of traditional spectroscopy setups become particularly pronounced. Recent developments in miniaturized Fabry-Pérot based interferometers have shown great potential for the miniaturization of spectrometers. Air-gap and liquid-gap filters focusing on low-order, small-gap concepts have been successfully achieved, often employing piezoelectric-based cavity length modulation systems [9–11]. While effective, these piezoelectric-based solutions come with some drawbacks, including complexity, sensitivity to vibrations, and maintenance requirements.

As an alternative, tunable solid-cavity Fabry-Pérot filters based on the thermo-optic effect (temperature-dependent refractive index changes) and thermal expansion have been explored [12,13]. Thermal tuning offers some advantages, such as simplicity, compactness, and lower maintenance requirements, which are critical for some applications, including miniaturized spectroscopy. However, this approach also presents challenges, particularly in environments with limited heat

* Corresponding author.
E-mail addresses: bruno.esteves@dei.uminho.pt (B. Esteves), b13742@cmems.uminho.pt (B.S. Dores), fsilva@dei.uminho.pt (M.F. Silva), higino.correia@dei.uminho.pt (J.H. Correia), jrodrigues@dei.uminho.pt (J.A. Rodrigues).

https://doi.org/10.1016/j.measurement.2025.118444
Received 18 October 2024; Received in revised form 23 June 2025; Accepted 14 July 2025
Available online 16 July 2025
0263-2241/© 2025 The Author(s). Published by Elsevier Ltd. This is an open access article under the CC BY license (http://creativecommons.org/licenses/by/4.0/).

dissipation, such as in high-vacuum environments. In these cases, additional design considerations, such as integrated heat dissipators, become necessary.

Despite significant progress, miniaturizing high-resolution filters, as required for Brillouin spectroscopy, remains a challenge. One of the main obstacles is maintaining parallel mirror alignment over the required cavity lengths, especially in tunable designs that typically require positional adjustments between the mirrors.

In this study, a new approach for achieving tunability in large-gap Fabry-Pérot interferometers is presented. This method revolves around the use of a solid glass resonance cavity, obtained from commonly available glass substrates, where the transmitted wavelength is controlled through temperature modulation (material expansion and changing refractive index). This allows for a monolithic device with no moving parts, where alignment between mirrors is guaranteed during fabrication, making it ideal for use outside of laboratory conditions. The use of these substrates as the resonance cavity results in a much larger cavity than that commonly achievable through the thin film deposition methods traditionally used to obtain solid resonance cavities, allowing for greater resolution.

The proposed device structure is represented in Fig. 1. It is comprised of a solid glass plate that serves as the resonance cavity, two Bragg reflectors (one fabricated on each side), and a metallic layer deposited on top of one of the mirrors, serving as a heating resistor for controlling the temperature of the device and as a mask for blocking undesired light transmission.

2. Methods

2.1. Fabry-Pérot theory

For a Fabry-Pérot filter, considering an incident beam perpendicular to the filter surface, the light transmission (T) for a given wavelength (λ) is determined by Eq. (1).

$$T_\lambda = \frac{t_0}{1 + \left(\frac{4F^2}{\pi^2}\right) \times \sin^2\left(\frac{2\pi Ln}{\lambda}\right)} \tag{1}$$

where t_0 is the maximum transmission (determined by losses in the system), F is the mirror finesse (depending on flatness and reflectivity), L is the cavity length, and n is the cavity refractive index. According to the equation, the transmission peak (λ_p) occurs for every wavelength that satisfies the condition given by Eq. (2), as shown in Fig. 2. As L and n are temperature-dependent, by modulating the temperature of the cavity it is possible to sweep λ_p across the spectrum, allowing for a tunable filter.

$$\lambda_p = \frac{2Ln}{p}, p \in \mathbb{N} \Rightarrow p = \frac{2Ln}{\lambda_p} \tag{2}$$

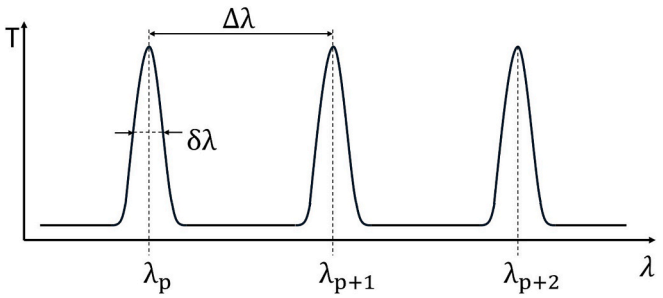


Fig. 2. Frequency/transmission representation for a Fabry-Pérot of order ≫1.

2.2. Cavity size limitations

For correct discretization of the desired spectral features, several considerations and limitations need to be evaluated, most related to the properties of the optical cavity. A larger L results in a larger resolution, as $\delta\lambda$ is inversely proportional to L (for $L \gg \lambda_p$). Despite $\delta\lambda$ decreasing with L (increasing resolution), as it is directly proportional to the free spectral range (FSR), there is a limit to L for this device linked to the spread of the target Brillouin spectrum (ΔB). Since the measured intensity is the sum of T_λ for all λ_p that satisfy the condition in Eq. (2), the entire wavelength spread of the case study must be smaller than $\Delta\lambda$, also known as the FSR (Eq. (3)), which is directly proportional to $\delta\lambda$, following the relation $F = \Delta\lambda/\delta\lambda$.

$$FSR = \lambda_p - \lambda_{p+1} = \frac{2Ln}{p} - \frac{2Ln}{p+1} = \frac{\lambda_p}{p+1} = \frac{{\lambda_p}^2}{2Ln + \lambda_p} \tag{3}$$

The upper limit of L is then defined by the relation FSR > Δ *B*, and the best theoretical filter will always be obtained by the largest L that satisfies the same condition. Taking the broader term for typically expected Brillouin signals as frequency shifts of up to 100 GHz, which, for 532 nm, corresponds to a spectral spread of approximately 189 pm (including the width of the Brillouin peaks, as this must be considered for the spread), filters with an FSR above 189 pm will be able to resolve the signal correctly. The closer the FSR is to this value, the higher the achievable resolution. For specific applications, systems are typically designed for narrower spectral spreads, determined by the maximum expected Brillouin shift for the intended application, meaning the optimal FSR will vary accordingly.

2.3. Cavity selection

As the transmitted wavelength of the filter depends on the distance between the mirrors, for a material of constant n, even slight thickness variations of a few nanometers can lead to an increase in $\delta\lambda$, decreasing the resolution. While achieving a flat surface with nanometer-level

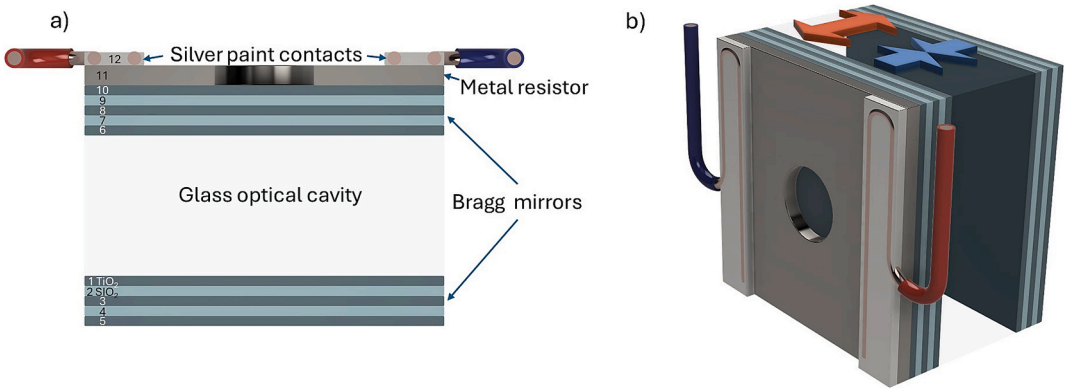


Fig. 1. Schematic of the proposed filter. a) Cross-section of the filter showing all the layers numbered by order of fabrication. b) Schematic of the full device.

flatness for an active area in the scale of mm^2 by polishing a glass substrate is feasible, intentionally grinding two flat surfaces separated by a solid glass plate while ensuring parallelism between them poses a greater challenge, not often discussed. Despite this difficulty, it was theorized that for several glass manufacturing methods, small areas of high parallelism, in the several mm^2 scale and suitable for use, must randomly occur inside larger regions of lower parallelism. A Fizeau interferometer was constructed to test this possibility. The device shown in Fig. 3, commonly used to study surface topography, projects an interferogram that consists of the interference pattern between the two surfaces of the glass slide (in this configuration one of the surfaces serves as the reference to the other), which is related to the relative thickness variation between the two [14]. A 200 mW, 532 nm continuous-wave laser (Oxxius L1C-532S) was used in this setup, as it is designed for extremely narrow spectral width (≤1 MHz) and high wavelength stability (<1 pm variation over 8 h under a 3 K temperature change), making it ideal for this and subsequent characterization setups.

In the interferogram, connected regions of the same intensity share the same thickness. Thickness variation is related to the intensity variation and is the same between every fringe (given by Equation (4).

$$\Delta L_F = \frac{\lambda_p}{2n} \tag{4}$$

This device is ideal for the substrate evaluation process, as the interferogram of the entire area is immediately visible, allowing rapid identification and elimination of substrates that present numerous fringes. Substrates with a minimum number of fringes (<10 mm between adjacent fringes) were selected for further evaluation using the open-source interferogram analysis software (DFTFringe) to find areas of low thickness variation.

Borosilicate glasses are known to express positive thermo-optic and thermal expansion coefficients for the relevant working temperatures, which facilitates the correlation between temperature and the observed shift in the transmission spectrum [15–18]. Several fabrication methods and thicknesses of borosilicate glass were tested, from commonly available microscope slides and cover glasses manufactured by the traditional float glass, rolling and drawing methods, to 2-side polished glass wafers. For all methods and thicknesses, it was possible to find glass plates with sufficiently consistent parallelism. The 2-side polished glass wafers showed the largest and most frequent adequate areas.

In this study, the selection of the tested glass was further guided by choosing thicknesses and refractive indexes that could result in adequate cover of the target Brillouin signal spread. Another consideration was maintaining the minimum temperature for achieving two consecutive orders of transmission below 200 °C, in order to facilitate mounting and maintain compatibility with the measuring devices for characterization. Two glass substrates were ultimately chosen for the early prototypes.

A 110 μm cover-slide (D 263 M borosilicate glass, Paul Marienfeld GmbH & Co.KG) with a refractive index of 1.5265 (for 532 nm) was selected for the fabrication of a filter with an FSR of 841.4 pm, covering the typical Brillouin spectral spreads with a significant margin. Finally, a 700 μm 2-side polished glass wafer (Borofloat33 borosilicate glass, MicroChemicals GmbH) with a refractive index of 1.4739 (for 532 nm) was also selected, this time for the fabrication of a filter with an FSR of 137.1 pm. This filter was designed to increase resolution by lowering the FSR, while still covering Brillouin spread of common biologic and polymeric samples.

Since surface roughness, along with surface parallelism, can influence filter performance, assessing substrate quality is crucial. A mechanical profilometer (Dektak 150, Veeco Instruments Inc.) was used to measure the root mean square roughness (Rq) of the selected substrates. Over a 100 μm linear scan, the cover slides exhibited an Rq of 1 nm, while the wafers showed Rq of 0.62 nm.

2.4. Bragg mirrors

Besides the quality of the Fabry-Pérot resonant cavity, the performance of the device, from the maximum and minimum transmission to $\delta\lambda$, is highly dependent on mirror quality, more specifically on mirror reflectivity and absorption. Bragg mirrors, which can achieve higher reflectivity than traditional metallic mirrors, were developed and used in the device [19]. These mirrors consist of N periods of alternating layers of high (TiO_2) and low (SiO_2) refractive index, all one-quarter wavelength thick (d), as seen in Equation (5), terminated by an additional layer of high refractive index (with the number of layers being 2 N + 1) [20].

$$d = \frac{\lambda_p}{4n} \tag{5}$$

TiO_2 (d = 52.99, n = 2.51) and SiO_2 (d = 90.66, n = 1.47) thin films were deposited by reactive sputtering and electron beam evaporation, respectively. The deposition processes were iterated until the ideal

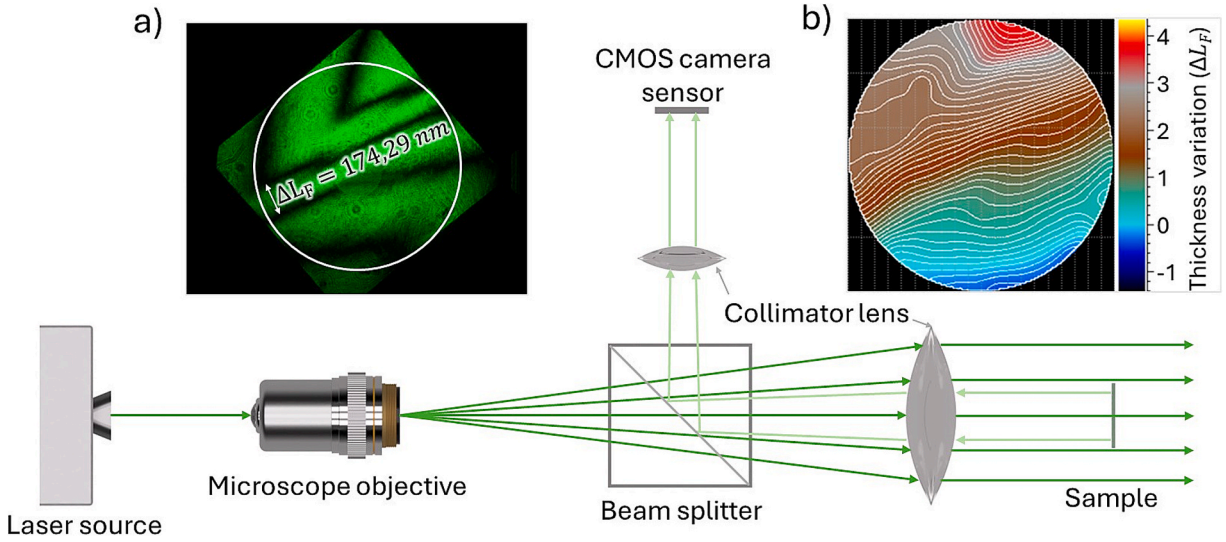


Fig. 3. Schematic of the Fizeau interferometer built to evaluate glass samples for face parallelism. The laser beam is expanded by the microscope objective (high numerical aperture lens) and collimated. The light reflected from the first surface of the sample interferes with the light reflected from the second surface and is directed by the beam splitter and collimated before reaching the camera sensor. a) Interferogram of a glass slide sample. b) Variation in the distance between the two glass surfaces obtained from DFTFringe.

characteristics of the thin films were consistently achieved. Thickness and refractive index were measured and optimized using an ellipsometer (alpha-SE, J.A. Woollam Co.) and the aforementioned mechanical profilometer was used to confirm thickness accuracy.

The reported ellipsometer was also used in transmission configuration to measure the transmittance of the fabricated Bragg mirrors.

2.5. Fabrication process

Two variants of the filter were fabricated, one using an 110 μm cover-slide and the other using a 700 μm 2-side polished glass wafer as resonance cavity material. Both substrates were selected due to containing large regions of uniform thickness, verified using the Fizeau interferometer. Different thicknesses were chosen to evaluate the impact of this parameter on filter performance and modulation.

For the Bragg mirrors, an N of 1 was chosen. As characterization was a priority for these initial prototypes, a low N allows for wider transmission peaks and a higher minimum transmission, which allows for lower demands on the resolution and sensitivity of the characterization setup, maintaining relevance for studying the effect of temperature modulation. While with an N of 1, these mirrors do not offer a significant improvement in reflectivity over metallic mirrors, Bragg mirrors were still preferred for the prototypes, since they still minimize absorption and can be easily altered by simply increasing the number of layers in each one to increase reflectivity and the resolution of the filter.

After the deposition of both mirrors, the Fizeau interferometer was used to identify the largest transmission region. The narrow spectral width of the laser used creates high-contrast transmission regions when observed from the transmission side of the interferometer. By positioning the filter on an optical mount and rotating it by fractions of a degree, thickness variations can be visualized with greater resolution compared to using the glass sample alone. Using this information, a circle of 1 mm was selected as the transmission region for each sample and masked on one side using a Kapton tape mask of the same dimension, in preparation for the deposition of the thin metallic film that serves as the resistor and light mask. Although much larger adequate regions can be found and utilized by enlarging the pinhole, a larger temperature gradient is created, limiting its size for this style of resistor.

For the filter with an optical cavity 700 μm thick, a 200 nm Ti layer deposited by DC sputtering was used as the resistor. Ti was chosen due to its strong adhesion properties, relatively high resistance among metals, and excellent heat stability.

Initially, the same resistor was applied to the first iterations of the thinner filters (110 μm optical cavity). However, despite initial stability, the thinner filters would suddenly break during handling or heating. This was attributed to structural tensions arising from different thin film deposition steps. Ultimately, for all 110 μm optical cavity filters, a 50 nm Al thin film deposited by electron beam evaporation was used instead. Although a thinner layer would better match the Ti resistors used for the 700 μm optical cavity filters, thinner Al layers do not block enough light to effectively serve as a light mask, so 50 nm Al layers were used.

After fabrication, the device was fixed on a 3D-printed flat support. One corner was directly fixed with Kapton tape, while the opposite corner was free to slide horizontally, being supported by a glass spacer also fixed with Kapton tape (Fig. 4). This arrangement allows the structure to expand in every direction without deforming and changing the incidence angle. One copper wire was attached to each side with silver conductive paint, completing the structure. Connection methods that use high temperatures were avoided to prevent permanent deformations on the glass surface. While the conductive paint provides sufficient adhesion for normal operation, a small portion of the wire near the connection point was secured to the mount with Kapton tape to enhance stability and prevent accidental disconnections during characterization.

Although this mounting approach was chosen to facilitate characterization, it is not required for normal operation. The monolithic construction inherently provides high mechanical stability, allowing the filter to function freely without the need for a specific mounting strategy. However, depending on the application, additional mounting solutions may be beneficial for ensuring precise alignment and minimizing unintended mechanical stresses.

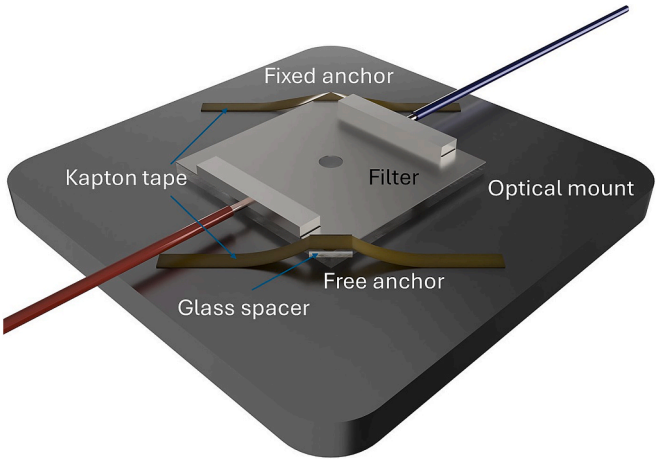


Fig. 4. Filter fixed to an optical mount using Kapton tape. One corner is fixed directly and the opposite corner is allowed to slide by using a glass spacer, which allows the filter to expand in all directions instead of deforming.

2.6. Device characterization

The peak transmission of the fabricated filters for 532 nm is of large order, and subsequently, the jump between transmission peaks of consecutive order is approximately constant. In this way, a change in n*L can be approximated to a shift in the transmission spectrum.

The narrow spectral width of the Oxxius L1C-532S laser makes it ideal for the characterization process. By fixing the incident light wavelength to a single line in the spectrum and inducing a shift in the transmission spectrum by heating the filter, a relation between temperature and transmission for 532 nm is created. Due to the large order of the filter, the resulting acquisition graph approximates what would be obtained by a sweep of the wavelength of the incident light viewed by a static filter, while here it is the transmission spectrum that suffers an approximately linear shift instead, while the emission source remains fixed.

The device was heated by applying a constant current to the resistor layer. Transmission was quantified using a calibrated photodiode (Hamamatsu S1336-8BK) and temperature was measured using a thermal camera (Optris PI 450). The mean temperature of the glass surface inside the resistor pinhole was used to characterize the device. The characterization setup is represented in Fig. 5.

3. Results and discussion

3.1. Bragg mirrors

The first filter prototypes were fabricated using Bragg mirrors with N = 1. However, mirrors with N ranging from 1 to 5 were also simulated, fabricated, and characterized. Simulations were conducted using optical models of the deposited SiO_2 and TiO_2 thin films, derived from ellipsometry measurements, to explore the potential resolution achievable with our process.

Fig. 6a) presents the ideal case for Bragg mirrors constructed from these thin films. The R (532 nm) was calculated as 0.7191, 0.8938, 0.9624, 0.987, 0.9955, for N = 1, 2, 3, 4, 5, respectively.

Fig. 6b) shows the measured reflectance of the fabricated Bragg mirrors. Since ellipsometry confirmed negligible absorption for both

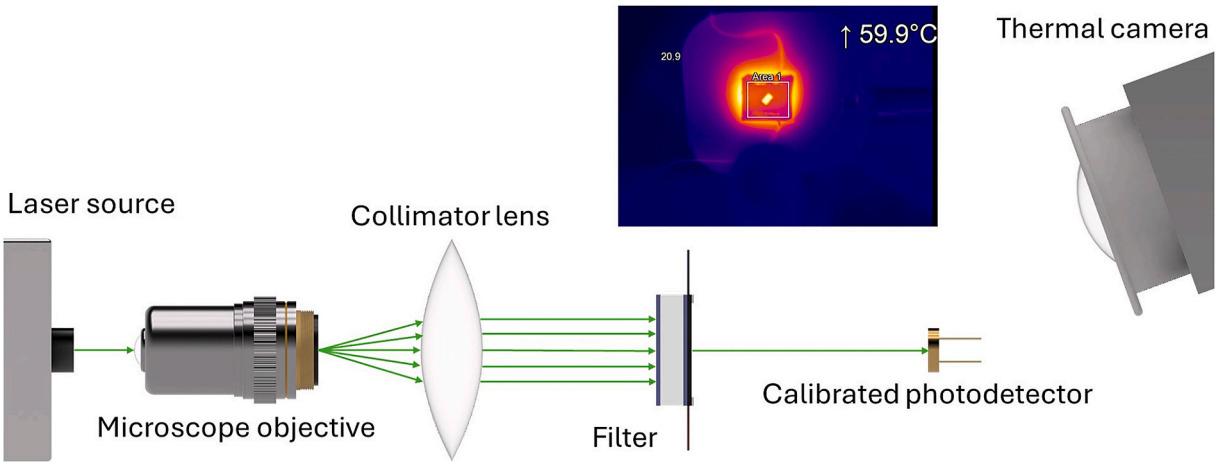


Fig. 5. Characterization setup used to correlate the temperature to the transmission of the developed filters.

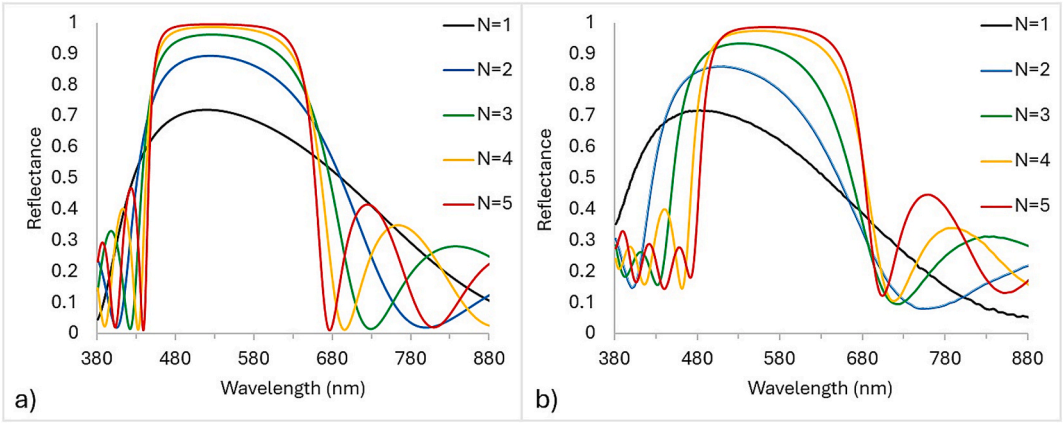


Fig. 6. a) simulated reflectance of bragg mirrors as a function of wavelength for different numbers of high/low refractive index pairs (n), using SiO_2 and TiO_2 models obtained from ellipsometry measurements of the deposited thin films. b) Measured reflectance of fabricated Bragg mirrors for N = 1 to 5. All simulations were performed in the OpenFilters software, incorporating the glass substrate to enhance comparability with real measurements.

SiO_2 and TiO_2, the reflectance was directly obtained from transmission measurements using the reported ellipsometer in transmission mode. The measured reflectance at 532 nm was found to be R = 0.6904, 0.851, 0.9333, 0.9696, 0.9807, for N = 1, 2, 3, 4, 5, respectively.

As observed in Fig. 6, there is a significant wavelength shift in the maximum reflectance between the simulated and fabricated mirrors. This discrepancy aligns with expected deviations in layer thickness and refractive index across different depositions. The increased minimum reflectance at specific wavelengths and the overall reduction in peak transmission further confirm this effect. Additionally, minor

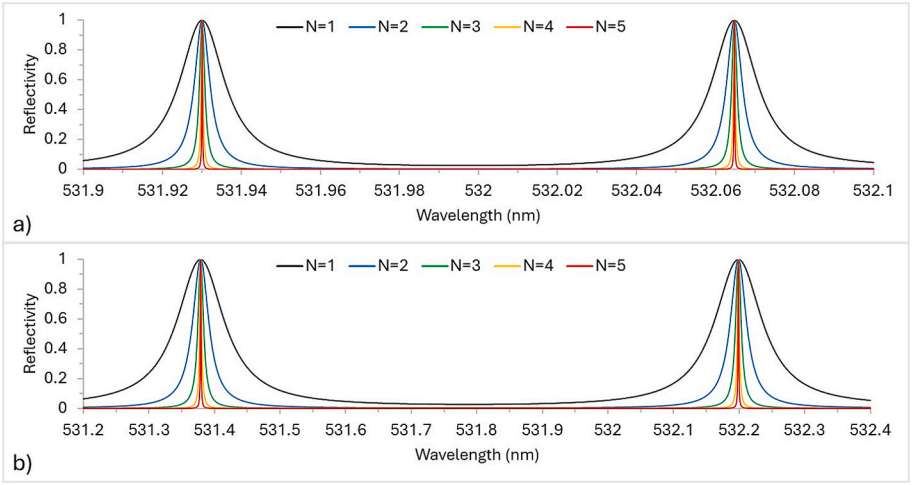


Fig. 7. Simulated transmittance spectra of Fabry-Pérot filters with cavity lengths of: a) 700 μm, and b) 110 μm.

inaccuracies in the SiO_2 and TiO_2 optical models, such as unaccounted residual absorption, particularly in TiO_2, can contribute to deviations between predicted and measured values. Despite these variations, the fabricated mirrors closely approximate the theoretical results and offer substantial improvements over metal mirrors for sufficiently high N.

3.2. Fabry-Pérot filters

The complete Fabry-Pérot filter was simulated for the 700 μm and 110 μm cavity prototypes, considering mirror layer counts up to N = 5, to assess the impact of mirror quality on finesse and spectral resolution. Fig. 7 presents the simulated transmission spectra for two adjacent transmission orders, for each filter.

As expected, increasing N reduces the linewidth of the transmission peaks and decreases the minimum transmittance, which complicates the characterization. This was a key factor in choosing N = 1 for the prototypes described.

To further evaluate the filter quality, the finesse of the simulated filters with N = 1 using the reported SiO_2 and TiO_2 layers, was calculated. The resulting values were 9.24 for the 700 μm cavity filter and 9.15 for the 110 μm cavity filter.

For characterizing the fabricated filters, the resistors were driven with constant current. For the 700 μm filter, a current of 450 mA was applied. Fig. 8 displays the resulting behaviour.

The filter was heated until 4 consecutive transmission peaks could be observed and then allowed to cool naturally. Significantly worse performance during the heating cycle was predicted due to uneven heating of the cavity caused by the pinhole in the resistor thin film and sharp temperature slope, which was confirmed through the experimental data. A significant decrease in the maximum filter transmission between the lowest temperature and subsequent transmission peaks was also observed, which is theoretically caused by a drop in mirror reflectivity due to the change of thickness and refractive index of the Bragg mirror layers. The effect is more pronounced during the heating cycle, since the Bragg mirrors constitute the outer layers of the structure, cooling faster than the glass cavity. The apparent shift between the cooling and heating cycles in Fig. 8b) is caused by the temperature measuring method, since the measured surface is in direct contact with the resistor thin film, creating a temperature gradient from which it is at the highest value.

Considering the maximum transmission points and the calculated free spectral range of the filter (137.1 pm), it is possible to create an accurate correlation between temperature and transmission frequency, as shown in Fig. 8c), where a wavelength shift of 5.7 pm/°C can be verified. The filter shows a linear correlation between temperature and transmitted wavelength for the tested temperatures. Although a larger number of peaks is necessary to characterize the behaviour of the filter, 2 peaks are sufficient to calibrate the device, as is commonly done in air–gap tunable Fabry-Pérot spectrometers, meaning that the filter can be fully operated with a temperature gradient <30 °C.

Since filter performance fluctuates with temperature, particularly during the heating cycle, a finesse value representative of the full operating range cannot be directly obtained. However, the linewidth of each transmission peak, calculated as the full width at half maximum (FWHM), provides insight into how finesse evolves with temperature. These results are presented in Fig. 9.

While widening of the transmission peaks was expected with an increase in temperature for the 700 μm optical cavity filter, the opposite trend was observed. Although the trend deviates significantly from a regular curve, its consistency across both heating and cooling cycles suggests that it reflects a real physical phenomenon rather than measurement artefacts.

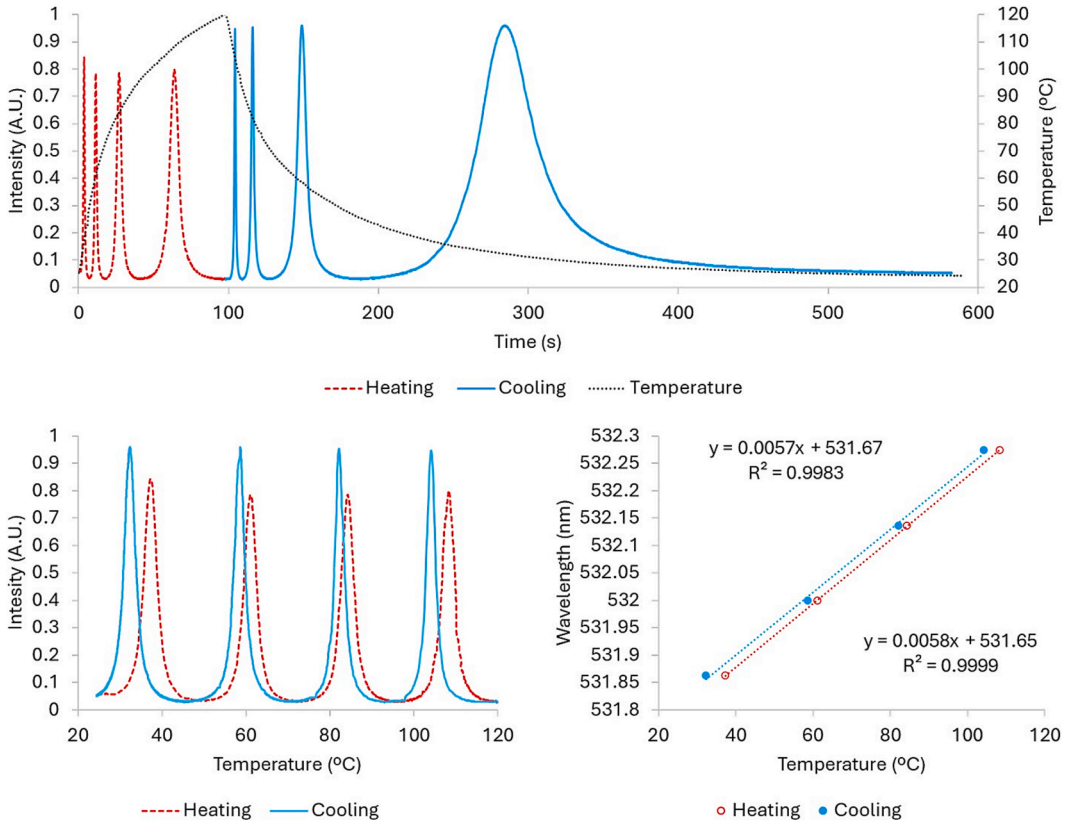


Fig. 8. Characterization of the 700 μm filter when a constant current of 450 mA is applied. a) Photodiode signal and mean temperature recorded on the glass surface in the pinhole over time. b) Correlation of the light intensity measured by the photodetector with the temperature. c) Calculated wavelength transmission shift with temperature for a single transmission peak.

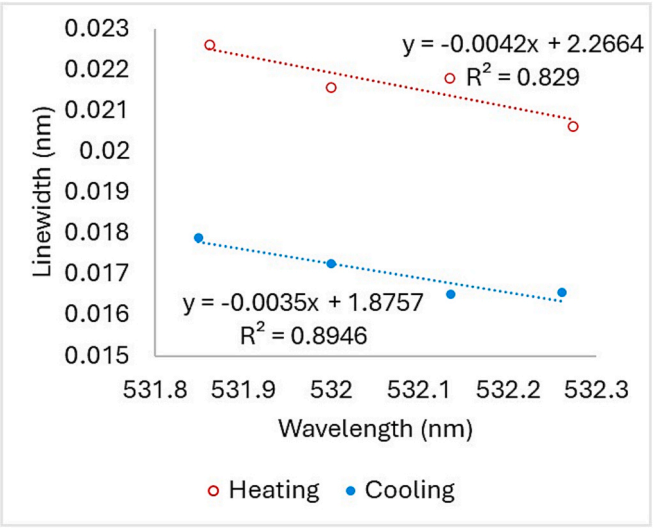


Fig. 9. Linewidth variation as a function of transmission peak wavelength for the 700 μm cavity filter.

Given that the characteristics of filter performance have shown some inconsistency with temperature, and can even vary in opposite trends, the cooling cycle closest to room temperature was chosen for calculating an estimate of finesse, yielding a value of 7.665. It is important to note that this value assumes that the filter maintains the referred performance throughout the entire working range during both heating and cooling cycles, which is not the case. Instead, it represents an idealized scenario where thermal gradients are minimized, and mirror degradation during heating is negligible, where the filter operates in and near the designed temperature range.

Considering the calculated results, measured finesse remains significantly lower than the simulated value, suggesting that further improvements can be achieved by optimizing cavity selection, such as further minimization of thickness variations and surface roughness, and by optimizing the mirror fabrication processes, namely minimizing the residual absorption of the thin films composing the Bragg mirrors.

One of the main advantages of this design is its stability due to its monolithic construction. To assess both long-term stability and potential thermal degradation, tests were conducted one year after initial characterization. Significant structural changes were not expected as the structure consists of stable oxides and a titanium resistor, which naturally resists oxidation after forming a thin protective oxide layer.

Nonetheless, a stress test was performed one-year post-fabrication. While normal operation involves cycling the filter between two transmission peaks, this test expanded the thermal range, cycling the device between 22 °C and 116 °C three additional times, allowing observation of two additional transmission peaks. The only notable change was a slight shift (1.3 °C) along the temperature axis compared to the profile recorded in Fig. 8b). This shift was anticipated, as the filter had been removed from its original testing position when not in use. Since precise realignment with the incident beam is challenging, small deviations naturally cause a minor global temperature shift in the measurements.

To account for this, the previously described calibration method for correlating temperature and transmitted wavelength was applied, aligning both curves to enable a direct comparison.

The results, shown in Fig. 10, confirm that the new characterization remains consistent with the original transmission spectrum. This indicates that the device is stable over time and does not experience significant degradation due to heating within its normal operating range.

Fig. 11 displays the 110 μm filter behaviour when applying a constant current of 4.5 A to the resistor.

The filter was heated until 2 consecutive transmission peaks could be observed and then allowed to cool naturally. As can be seen in Fig. 11a) and b), the same differences between the heating and cooling cycles are present, accentuated due to an higher maximum temperature. At the end of the heating cycle, a small crack was observed to form on the glass substrate. During cooling, the crack visible widened with a noticeable sound. Two artifacts can be observed in the signal, one during the heating cycle and another during the cooling cycle, theoretically corresponding to the reported formation of small cracks in the glass layer. This proposition is reinforced by an inverse shift between the heating and cooling cycles, indicating a slight change in the angle of incidence due to the release of tension in the structure. Furthermore, for this filter, flatness was significantly affected during the heating cycle, as observed in a section of the reflected collimated light.

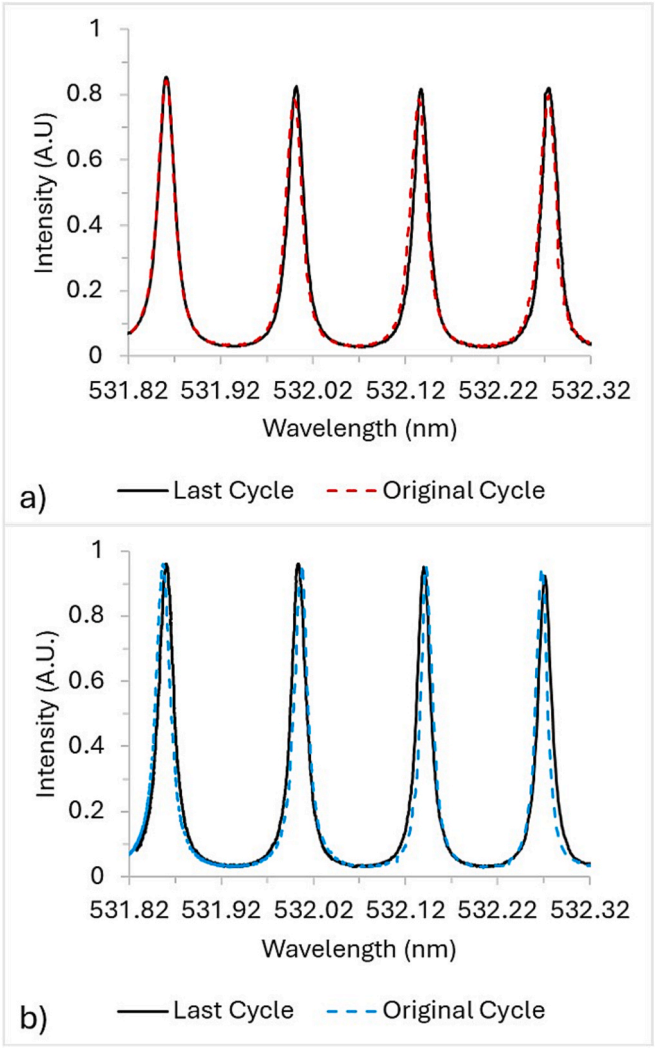


Fig. 10. Comparison between the original and the last thermal cycles performed 364 days apart. a) corresponds to the 450ma current application and heating, while b) corresponds to the posterior cooling process.

Although observing more than 2 consecutive transmission peaks was not feasible (due to the need of unreasonable temperatures for device operation and integrity), similar behaviour to the 700 μm filter is expected. Therefore, a linear fit was applied between the two maximum transmission points, considering the calculated spectral range (841.4 pm).

This result shows that the 110 μm filter is close to the thickness lower limit for this device when using this material as the resonance cavity. The higher temperature required compromises the integrity of the device and affects the mounting hardware, leading to alignment issues and hindering the characterization of the wavelength transmission/

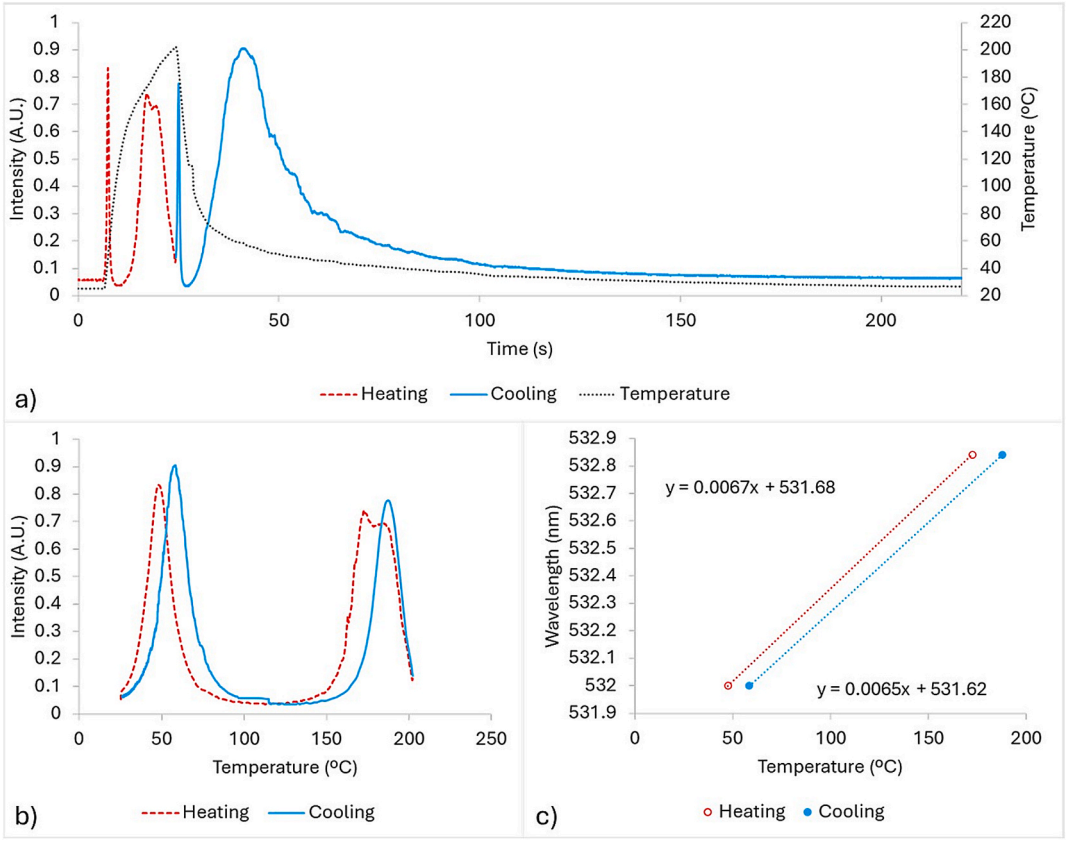


Fig. 11. Characterization of the 110 μm filter when a constant current of 4.5 A is applied. a) Photodiode signal and mean temperature recorded on the glass surface in the pinhole over time. b) Correlation of the light intensity measured by the photodetector with the temperature. c) Estimated wavelength transmission shift with temperature for a single transmission peak.

temperature curve. In contrast, the 700 μm filter demonstrates promising performance. Despite some variability, the peak transmission remains relatively constant, especially during the cooling cycle, indicating that mirror parallelism is naturally preserved when thermal gradients in the optical cavity are reduced. Furthermore, the filter demonstrates a highly linear response while maintaining a reasonable working temperature. As the structure was fractured during the described characterization, no further testing regarding long term stability and thermal degradation could be performed on this prototype.

Using the same approach as for the 700 μm filter, Fig. 12 presents the linewidth evolution for the 110 μm cavity filter. For this filter linewidth increased in temperature, as expected. In this case, the linewidth increases with temperature, as expected. It is worth noting that during the second heating cycle, the previously mentioned artefact significantly affects the transmission peak shape, contributing to an increased measured linewidth.

For this filter, again, the cooling cycle transmission peak closest to room temperature was used for calculating fineness, resulting in a value of 6.786. Given the significantly higher temperature variation within transmission peaks compared to the 700 μm filter, a lower finesse was expected. The increased linewidth is attributed to the degradation of cavity uniformity and mirror quality. Additionally, the observed sudden fracture may have also contributed to this result, as the selected peak occurred after the event.

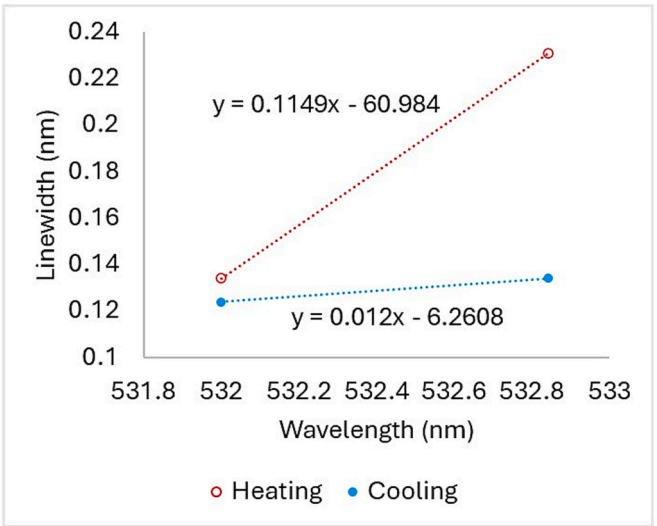


Fig. 12. Linewidth variation as a function of transmission peak wavelength for the 110 μm cavity filter.

3.3. Optical resonance cavity considerations

During operation, the performance of the Fabry-Pérot filter is directly influenced by the heating process. Thermal expansion and thermo-optic effect, which serve as the driving mechanisms, can impact the filter's performance if these effects are unevenly distributed across the cavity. In addition to altering the cavity properties, temperature gradients may also affect the mirrors. While peak splitting caused by spatially dependent transmission variations or mode degeneracy loss is not immediately apparent, peak broadening is evident, as the finesse varies considerably during the heating process.

Isolating the individual contributions of thermal expansion and thermo-optic effect to peak degradation and filter transmission is

challenging, as these factors are interdependent. However, it is clear that thermal gradients negatively impact filter performance. Minimizing such gradients by optimizing the resistor placement and geometry becomes a priority. In this context, the dimensions of the active transmission area are particularly relevant, as they strongly influence the spatial extent and impact of thermal non-uniformities.

To further investigate the significance of the cavity dimensions, the 10 mm × 10 mm × 700 µm prototype fabrication process was repeated four times, without the deposition of the Bragg mirrors, varying only the diameter of the optical cavity (1 mm, 2 mm, 3 mm, and 4 mm). As the samples were suspended from the two connecting wires for temperature measurements, small strips of Kapton tape (around 1.2 mm width) were wrapped around the corners to reinforce the connections. For heating, direct current was supplied until the maximum temperature registered inside the optical cavity stabilized at 70 °C. This target temperature was selected because, under an ambient temperature of 20 °C, it is sufficient to fully resolve two successive transmission peaks in the 700 µm cavity filter, based on observed experimental behaviour. Thermal images were captured using the aforementioned thermal camera, and the results are shown in Fig. 13.

On the resistor side, only the glass surface of the optical cavity can be measured accurately, as the metallic surface has a low emissivity. This limits the ability of the thermal camera to register its true temperature, often causing the metal to appear cooler than it actually is. While this natural contrast helps isolate and identify the optical cavity, a crosstalk effect from adjacent pixels at the resistor-cavity boundary creates an artificial ring of lower temperatures around the cavity for all diameters. Additionally, for the 1 mm and 2 mm cavities, the camera's resolution further hinders analysis due to the reduced target area and thermal gradients.

Despite these challenges, several conclusions can be drawn from the thermal imaging. It was initially expected that the thermal gradient

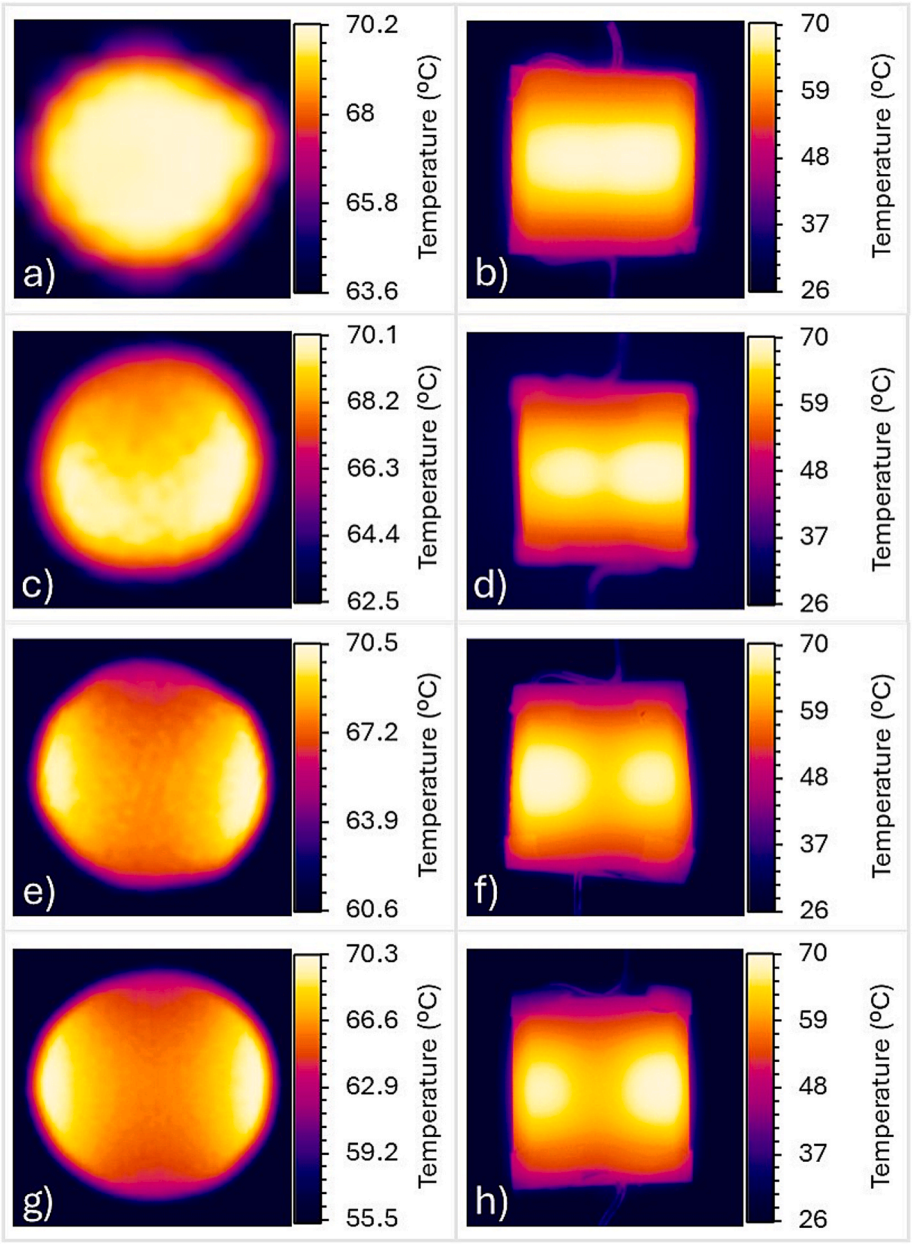


Fig. 13. Thermal images of the optical cavity surface (resistor side, close-up) and the back surface of the glass substrate for different cavity diameters. a), c), e), and g) show the thermal distribution on the resistor side for 1 mm, 2 mm, 3 mm, and 4 mm cavities, respectively. b), d), f), and h) correspond to the backside of the glass for the same cavity sizes. All images were acquired in the same orientation.

across the cavity surface would be radially symmetric, with higher temperatures further from the center. However, this was not entirely observed. While a clear horizontal gradient is present, the vertical gradient is less pronounced and even appears to slightly reverse for the larger cavities. Examining the backside images of the substrate reveals two factors contributing to this. For larger cavities, the resistor's cross-sectional area is significantly reduced at the cavity, increasing electrical resistance at the sides of the resistor, which was predicted. Additionally, thermal dissipation from the copper wire connections can be observed in all samples, which was more significant than expected. While this effect could be mitigated by using thinner copper wire, ideally dimensioned to heat at the same or a closer rate as the resistor, it does not appear significant for the 1 mm cavity used in the described prototypes.

Regarding the effect of cavity size on thermal gradients, a clear increase in gradient intensity with diameter is observed, aligning with theoretical predictions.

Since the resolution of the thermal camera is insufficient to accurately analyse the 1 mm diameter cavity used in this study, a finite element thermal simulation was conducted which also provides insight into the expected thermal gradients within the optical cavity. The simulation, shown in Fig. 12, was also performed with a target resistor temperature of 70 °C.

As shown in Fig. 14, a uniform vertical temperature gradient is observed directly beneath the resistor surface, which would have minimal impact on filter performance. However, within the optical resonance cavity, significant lateral and uneven vertical thermal gradients are observed, with a maximum temperature gradient of 0.4 °C. This highlights the challenges of using a single resistor across the filter surface, as the resulting uneven thermal gradients can affect both refractive index and thickness uniformity. While this simulation represents the system after thermal equilibrium is reached, rapid heating cycles are likely to exacerbate these issues.

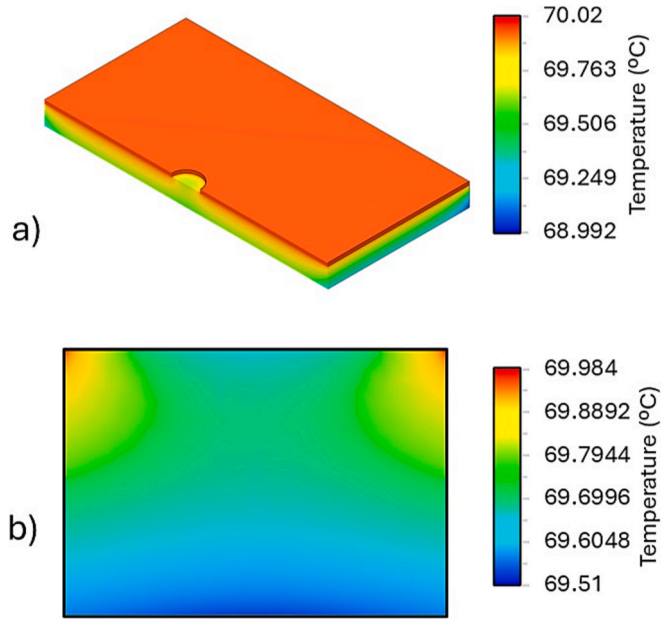


Fig. 14. Finite element thermal simulation of the current filter geometry at a target resistor temperature of 70 °C. The simulation considers convection at an ambient temperature of 20 °C, using a convection coefficient of 10 W/(m^2·K). Thermal conduction is modeled using a thermal conductivity of 16 mW/(mm·°C) for Ti and 1 mW/(mm·°C) for glass, along with a specific heat capacity of 523 J/(kg·°C) for Ti and 750 J/(kg·°C) for glass. Radiation is modeled with an emissivity of 0.9 for Ti and 0.3 for glass. a) Cross-section of the full filter geometry, consisting of a 10 × 10 × 0.7 mm glass substrate with a resistor covering the entire surface, excluding a 1 mm diameter central region. b) Cross-section of the resulting 1 × 0.7 mm optical cavity, corresponding to the uncoated central region.

Considering that miniaturization was one of the primary goals of this approach, the same configuration was simulated, reducing the substrate to a radial expansion of the optical cavity to support a smaller ring heating resistor. Two additional configurations were also explored: the first incorporated a second ring heating resistor on the opposite face of the filter, while the second employed the resistor radially around the axis of incidence, positioned on the wall of the filter, with the glass substrate reduced to consist solely of the optical cavity. For comparison, all optical cavities were modelled as 700 μm high and 1 mm in diameter cylinders. The geometries were dimensioned to ensure consistent resistor area across all configurations. The results of these simulations are presented in Fig. 15.

As shown in Fig. 15, thermal gradients within the optical cavity can be significantly reduced by modifying the resistor geometry and its location relative to the cavity. Configurations b) and c) show notable improvements, with maximum temperature gradients of 0.263 °C and 0.179 °C within the cavity, respectively, compared to configuration a), which has a maximum gradient of 0.728 °C. However, as shown in Fig. 15, lateral and uneven thermal gradients are still present, albeit at lower amplitude. Additionally, the best performing configuration (c) presents several challenges for fabrication, especially when using physical vapor deposition techniques for thin film deposition.

The spot size of the incident beam can also be modulated to reduce the impact of thermal gradients on the transmission spectrum, particularly from regions bordering the resistor, where thermal gradients are more pronounced. By decreasing the beam diameter, the incident beam avoids high-gradient zones, potentially resulting in improved peak definition. However, reducing the incident area below approximately 1 mm in diameter may significantly increase angular divergence, which strongly affects Fabry–Pérot filter behaviour due to their sensitivity to incidence angle.

Since both effects (gradient avoidance and angular dispersion) are non-trivial to quantify and cannot easily be analysed independently, no experimental variation of spot size was yet pursued. Nonetheless, this remains a promising avenue, especially for filters with larger optical apertures, where a modest reduction in beam diameter may effectively exclude high-gradient regions while maintaining acceptable angular dispersion.

Ultimately, an alternative configuration could further mitigate thermal gradients, particularly for optical cavities with a larger area, without significantly increasing fabrication complexity. By using transparent conductors, that eliminate the need for pinholes, and extending the substrate beyond the cavity region, planar resistors can be placed on both parallel faces to maximize temperature uniformity within the optical cavity. This approach was simulated and is illustrated in Fig. 16Fig. 12. The substrate is the same as for Fig. 15b) to facilitate comparison, as they are similar. With this approach, the maximum thermal gradient within the cavity is reduced to 0.075 °C. Even for thicker optical cavities, the thermal gradients produced by this configuration remain primarily vertical and uniform across the cavity area, minimizing their impact on filter performance. Ideally, the conductive material used for the resistor should have a high refractive index and replace the final H layer of the Bragg mirrors on each side.

Transparent resistors do not inherently block light outside the desired transmission region; however, an additional opaque layer can be easily deposited using the same fabrication process as the one used for the Ti and Al resistors.

To further enhance the filter's performance, Al, Ti, and transparent resistor versions can be calibrated and used as temperature sensors, allowing for continuous monitoring. This temperature data can then serve as feedback for a PID control loop, enabling precise regulation of the filter temperature and controlled heating and cooling ramps.

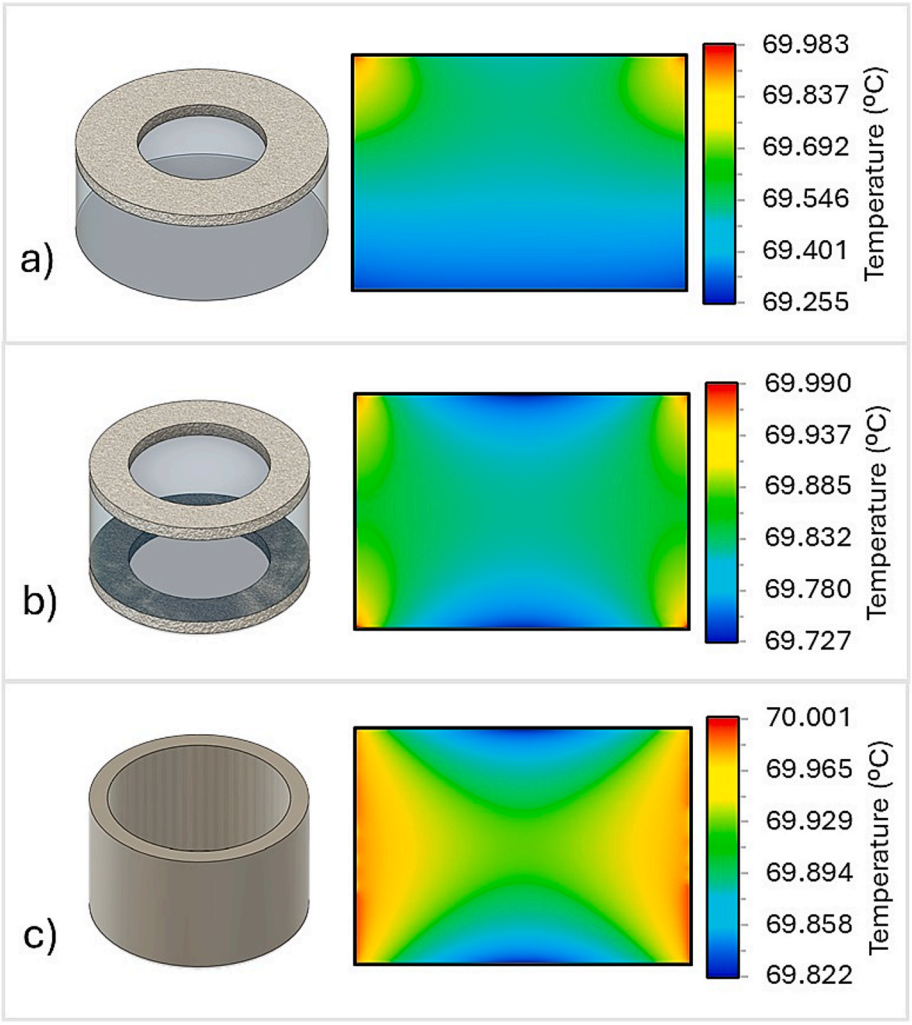


Fig. 15. Thermal simulation of the effect of different resistor configurations on the thermal gradient within the optical cavity. The simulations represent cross-sections of the resulting 1 × 0.7 mm optical cavity. a) Fabricated geometry after cutting the filter into a cylinder with a radius of $\sqrt{0.95}$ mm. b) Addition of a second heating resistor on the opposite face of the first one, with the filter cut into a cylinder of radius $\sqrt{0.6}$ mm. c) Addition of the heating resistor radially to the axis of incidence, with the substrate cut into a cylinder of radius 0.5 mm. The reported dimensions were chosen to ensure that the contact area between the resistor and substrate was the same for all filters. Thermal conduction, convection and radiation parameters were the same as those reported in Fig. 13.

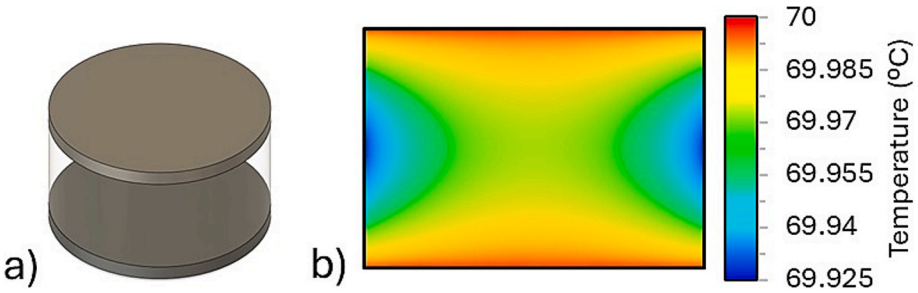


Fig. 16. Thermal simulation of the effect on thermal gradients of transparent resistors replacing the final H layer in the Bragg mirror. Thermal conduction, convection and radiation parameters were the same as those reported in Fig. 13. The transparent resistor was defined with the same physical properties as Ti to facilitate comparison. a) Geometry in use, where the substrate corresponds to a cylinder of radius $\sqrt{0.6}$ mm and height of 0.7 mm. b) Cross-section of the resulting 1 × 0.7 mm optical cavity.

4. Conclusions

A method for fabricating large-gap, monolithic, and temperature-tunable Fabry-Pérot filters using commonly available unaltered glass substrates as the resonance cavity was developed. This method can produce filters with large active area and large cavity length, suitable for high-resolution spectroscopy applications.

Several commonly available glass substrate types were tested and a method for analysing and selecting suitable parts using interferogram analysis was developed. Although adequate substrate selection, which is critical, can be a tedious and time-consuming process, the optimizations reported here significantly reduce this time.

The presented fabrication process achieves a tunable filter with no moving parts or actuators, designed for simplicity of fabrication and operation, compactness, robustness, and adaptability for several applications.

From the fabricated versions, the 700 μm thick solid glass resonance cavity filter achieved highly linear correlation between temperature and transmitted wavelength (transmission wavelength shift of 5.7 pm/°C, FSR of 137.1 pm), maintaining good performance throughout the working temperature range, especially for slow temperature changes, proving that the two mirrors maintain their parallelism naturally.

In conclusion, this work demonstrates that this technology may be suitable for miniaturization of spectrometers, specifically for high-resolution techniques, such as Brillouin spectroscopy, by demonstrating optical filters with significant advantages compared to available alternatives, such as low development and fabrication cost, low-maintenance, and high-performance.

Declaration of competing interest

The authors declare that they have no known competing financial interests or personal relationships that could have appeared to influence the work reported in this paper.

Acknowledgements

This work was supported by: (i) MPhotonBiopsy, PTDC/FIS-OTI/1259/2020 (http://doi.org/10.54499/PTDC/FIS-OTI/1259/2020) and (ii) CMEMS-UMinho UIDB/04436.

B. Esteves thanks FCT (Fundação para a Ciência e a Tecnologia) for the PhD grant 2021.07239.BD (http://doi.org/10.54499/2021.07239.BD).

B. Dores thanks LABBELS—Associate Laboratory in Biotechnology, Bioengineering and Microelectromechanical Systems, LA/P/0029/2020.

M. F. Silva thanks FCT for his contract with reference CEECINST/00156/2018/CP1642/CT0004 (https://doi.org/10.54499/CEECINST/00156/2018/CP1642/CT0004).

J. A. Rodrigues thanks FCT for his contract with reference 2023.06261.CEECIND/CP2841/CT0011 (https://doi.org/10.54499/2023.06261.CEECIND/CP2841/CT0011).

Data availability

No data was used for the research described in the article.

References

[1] F. Palombo, D. Fioretto, Brillouin light scattering: applications in biomedical sciences, Chem. Rev. 119 (2019) 7833–7847, https://doi.org/10.1021/acs.chemrev.9b00019.

[2] C. Poon, J. Chou, M. Cortie, I. Kabakova, Brillouin imaging for studies of micromechanics in biology and biomedicine: from current state-of-the-art to future clinical translation, J. Phys. Photon. 3 (2021), https://doi.org/10.1088/2515-7647/abbf8c.

[3] F. Scarponi, S. Mattana, S. Corezzi, S. Caponi, L. Comez, P. Sassi, A. Morresi, M. Paolantoni, L. Urbanelli, C. Emiliani, L. Roscini, L. Corte, G. Cardinali, F. Palombo, J.R. Sandercock, D. Fioretto, High-performance versatile setup for simultaneous Brillouin-Raman microspectroscopy, Phys. Rev. X 7 (2017) 1–11, https://doi.org/10.1103/PhysRevX.7.031015.

[4] B. Esteves, A. Rocha, M.F. Silva, J.H. Correia, J.A. Rodrigues, Non-contact determination of the viscoelastic properties of agar culture media by Brillouin spectroscopy, Materialia 30 (2023) 101858, https://doi.org/10.1016/j.mtla.2023.101858.

[5] J. Shi, D. Yuan, S. Hao, H. Wang, N. Luo, J. Liu, Y. Zhang, W. Zhang, X. He, Z. Chen, Stimulated Brillouin scattering in combination with visible absorption spectroscopy for authentication of vegetable oils and detection of olive oil adulteration, Spectrochim. Acta - Part a Mol Biomol. Spectrosc. 206 (2019) 320–327, https://doi.org/10.1016/j.saa.2018.08.031.

[6] G. Scarcelli, S. Besner, R. Pineda, P. Kalout, S.H. Yun, In Vivo Biomechanical Mapping of Normal and Keratoconus Corneas, JAMA Ophthalmol. 133 (2015) 480, https://doi.org/10.1001/jamaophthalmol.2014.5641.

[7] F. Palombo, M. Madami, D. Fioretto, J. Nallala, H. Barr, A. David, N. Stone, Chemico-mechanical imaging of Barrett's oesophagus, J. Biophoton. 9 (2016) 694–700, https://doi.org/10.1002/jbio.201600038.

[8] R.J.J. Rioboó, N. Gontán, D. Sanderson, M. Desco, M.V. Gómez-Gaviro, Brillouin spectroscopy: from biomedical research to new generation pathology diagnosis, Int. J. Mol. Sci. 22 (2021), https://doi.org/10.3390/ijms22158055.

[9] T. Jeon, A. Nateghi, W.M. Jones, C. Choi, J.P. Cardenas, C. Ross, A. Scherer, Development of a compact and robust mid-infrared spectrometer by using a silicon/air hyperspectral filter, ACS Photon. 9 (2022) 68–73, https://doi.org/10.1021/acsphotonics.1c01750.

[10] H. Tong, Y. Xiong, H. Ding, Z. Chen, Z. Qin, W. Chen, J. Tang, S. Yu, F. Xu, Lithium niobate piezoelectric actuator-integrated fiber fabry-pérot tunable filter with ultrahigh speed and linearity, ACS Photon. (2023), https://doi.org/10.1021/acsphotonics.3c01740.

[11] M.M.I. Tusher, H. Lee, S. Lee, K. Lee, Development of a miniaturized PZT-based MEMS Fabry-Perot interferometer with eutectic wafer bonding and its interface electronics, Sens. Actuat. A Phys. 366 (2024) 114934, https://doi.org/10.1016/j.sna.2023.114934.

[12] D. Hohlfeld, M. Epmeier, H. Zappe, Tunable thermo-optic filter for WDM applications, Proc. IEEE Micro Electro Mech. Syst. (2002) 564–567, https://doi.org/10.1109/memsys.2002.984334.

[13] K. Wu, Z. Li, J. Guo, Y. Xiao, H. Qi, W. Dong, S. Ruan, W. Chen, Y. Chen, Design of thermo-optic tunable optical filter based on Si/Air DBR and polymer Fabry-Perot microcavity in SOI, Optik (Stuttg). 125 (2014) 2885–2890, https://doi.org/10.1016/j.ijleo.2013.11.047.

[14] T.T. Kajava, H.M. Lauranto, R.R.E. Salomaa, Fizeau interferometer in spectral measurements, J. Opt. Soc. Am. B 10 (1993) 1980, https://doi.org/10.1364/josab.10.001980.

[15] A.C.P. Rocha, J.R. Silva, S.M. Lima, L.A.O. Nunes, L.H.C. Andrade, Measurements of refractive indices and thermo-optical coefficients using a white-light Michelson interferometer, Appl. Opt. 55 (2016) 6639, https://doi.org/10.1364/ao.55.006639.

[16] J.M. Jewell, Thermooptic coefficients of some standard reference material glasses, J. Am. Ceram. Soc. 74 (1991) 1689–1691, https://doi.org/10.1111/j.1151-2916.1991.tb07162.x.

[17] SCHOTT, BOROFLOAT®, Inf. Web Page (n.d.). https://www.schott.com/en-vn/products/borofloat-p1000314 (accessed May 6, 2024).

[18] SCHOTT, D 263®, Inf. Web Page (n.d.). https://www.schott.com/en-th/products/d-263-p1000318 (accessed May 6, 2024).

[19] W. Heiss, T. Schwarzl, J. Roither, G. Springholz, M. Aigle, H. Pascher, K. Biermann, K. Reimann, Epitaxial Bragg mirrors for the mid-infrared and their applications, Prog. Quant. Electron. 25 (2001) 193–228, https://doi.org/10.1016/S0079-6727(01)00011-8.

[20] I.-W. Feng, S. Jin, J. Li, J. Lin, H. Jiang, SiO_2/TiO_2 distributed Bragg reflector near 1.5 μ m fabricated by e-beam evaporation, J. Vac. Sci. Technol. A Vacuum, Surfaces, Film. 31 (2013) 2–6, https://doi.org/10.1116/1.4823705.